

1 **Dear Editor,**

2 **We would like to thank the reviewers for their help that improves the readability of this**
3 **paper. The reviews and our responses (in bold) are given hereafter. All the asked**
4 **corrections are highlighted in the text.**

5

6 **Reviewer 1**

7 In all paper the authors should abandon the use of BER, and adopt ONLY the LR values, as
8 done in all other papers published from non-French groups.

9 **As we wrote in response to the prior review, in the article we consider BER rather than**
10 **the lidar ratio (LR) which is the inverse of BER because it is directly proportional to**
11 **both the single scattering albedo and the probability to backscatter a photon. The use of**
12 **BER is not a scientific error. Moreover, the values of the corresponding lidar ratio (LR)**
13 **are indicated in parentheses for several cases, as in the abstract.**

14

15 This section is too long, and repeats same text as in the cited papers. Please shorten without
16 repetitions.

17 **Yes, we agree. The text has been shortened in the interest of clarity.**

18

19 It is better to use "linear particle" instead of "particulate"

20 **Yes, the correction has been done.**

21

22 The accuracy of the Microtops II retrievals has to be mentioned

23 **We have added the accuracy of the Microtops II.**

24

25 Replace "families" by "types"

26 **The correction has been done.**

27

28 **As these values are not unique for the aerosol types considered, I would like to see the**
29 **standard deviation (STD) values reported from other papers (to be cited). For instance the**
30 **marine type lidar ratio (LR) may vary from ... to and the LPDR values from 0 to .. %.**

31 **Ranges of values previously published in the literature have been added with the**
32 **references. The corresponding section has been highlighted in yellow in the modified**
33 **manuscript hereafter.**

34

35 Please use 1 word: nighttime

36 **The correction has been done.**

37

38 **Please cite relevant papers (e.g. detection of BB over Europe)**

39 **Previous papers have been cited: Fiebig et al. (2003), Müller et al. (2005), Groß et al.**
40 **(2011), Nisantzi et al. (2014). The corresponding section has been highlighted in green in**
41 **the modified manuscript hereafter.**

42

43 I find the Fig, 8b, full of very large discrepancies; thus no real information can be extracted. It
44 should be omitted (but discussed in the manuscript).

45 **We have a different opinion: it is also very important to show the data when a bad**
46 **agreement is highlighted, especially when the measurements are largely used in the field**
47 **with no precaution. We thus kept Fig. 8b as is.**

48

49 **Discuss how this compares with previous similar measurements.**

50 **As explained, a full explanation is given in the companion paper of Ancellet et al. (2016)**
51 **accepted in this issue. The corresponding section has been highlighted in pink in the**
52 **modified manuscript hereafter.**

53

54 **Be careful here> Over Cyprus the dust LR is lower than that from Saharan. This should be**
55 **mentioned and clarified here.**

56 **This point has been clarified in the text and another comparison has been added with**
57 **this reference. The corresponding section has been highlighted in blue in the modified**
58 **manuscript hereafter.**

59

60 **Reviewer 2**

61 This reviewer agree that co-located lidar and Cimel measurement data at Menorca Island are
62 very unique. However, a context in sections 3.1 and 3.2 is similar to the contents of

63 conventional papers, especially published by the authors. The quality of this paper will be
64 enhanced if the authors highlight the major findings of this work compare to previous papers
65 from the study region. In addition, some sentences should be concisely written. Same (or
66 similar) expressions and/or words were too often repeated.

67 **We have tried to be more concise and have rewritten some parts of the mentioned**
68 **sections for better clarity.**

69 If the aerosol optical and physical data from ground-based in-situ or airborne measurements
70 during the campaign are available, please add them to in this work (e.g. line 23-26 of page
71 32731).

72 **Yes, there were some in-situ measurements close to the ground. These values were found**
73 **to be irrelevant for comparison with the lidar profiles because they are mainly**
74 **representative of very local sources. The ground-based station is close to the sea and**
75 **very influenced by sea spray. The temporal evolution of the aerosol properties observed**
76 **in the tropospheric column is not marked at the ground level. Contrariwise, the**
77 **integrated measurements of the in situ sunphotometer are relevant and accounted for.**

78

79 To get more general conclusion, the comparison between SEVIRI and Cimel at Menorca
80 should be made with long-term data, not for only the intensive period data (Fig. 8).

81 **The objective is not to draw a general conclusion. The calibration and validation of**
82 **spaceborne instrument are made at the global scale, using for example all the ground-**
83 **based sunphotometers. On this base, the calibration may be correct. Nevertheless such**
84 **general consideration can be put in default for regional cases. The discrepancy that can**
85 **be observed could also be a function of the season. It cannot be investigated at length**
86 **here. The goal for this paper was only to verify the agreement of the SEVIRI-derived**
87 **aerosol optical properties with our measurements. We have corrected them before**
88 **building regional AOT map. The correction determined here is not necessary true for**
89 **other applications. We have specified this point.**

90

91 Section 4: If the aerosol type classification from CALIOP are available along the backward
92 trajectory, please add it.

93 **Yes, they are. For the pollution aerosol situations, the AOT is small and aerosol mixings**
94 **are present in the atmospheric column. In such condition, the aerosol typing derived**
95 **from CALIOP is not reliable. We have checked the aerosol identification of CALIOP for**
96 **the events of desert dust and biomass burning aerosols. The first one is well identified as**
97 **polluted dust. It is not shown in the paper but we have added a sentence. For the second**
98 **one, the description is given in the companion paper of Ancellet et al. (2016), as**
99 **explained in the text. The plume is identified over the Atlantic Ocean as a smoke and**
100 **polluted dust. We have added this information in the text.**

101 **Temporal consistency of lidar observables during aerosol transport events in the**
102 **framework of the ChArMEx/ADRIMED campaign at Menorca Island in June 2013**

103 **P. Chazette¹, J. Totems¹, G. Ancellet², J. Pelon² and M. Sicard³**

104 ¹LSCE, CEA-CNRS-UVSQ, UMR 8212, Gif-sur-Yvette, France

105 ²Sorbonne Universités, UPMC Université Paris 06, CNRS-UVSQ, UMR 8190 LATMOS, Paris, France

106 ³RSLab/IEEC-CRAE, Universitat Politècnica de Catalunya, Barcelona, Spain

Mis en forme : Anglais (États Unis)

107 **Abstract.**

108 We performed synergetic daytime and nighttime active and passive remote sensing
109 observations at Menorca (Balearic Island, Spain), over more than 3 weeks during the
110 Chemistry-Aerosol Mediterranean Experiment / Aerosol Direct Radiative Effect in the
111 Mediterranean (ChArMEx/ADRIMED) special observation period (SOP 1a, June-July 2013).
112 We characterized the aerosol optical properties and type in the low and middle troposphere
113 using an automated procedure combining Rayleigh-Mie-Raman lidar (355, 387 and 407 nm)
114 with depolarization (355 nm) and AERONET Cimel[®] sun-photometer data. Results show a
115 high variability due to varying dynamical forcing. The mean column-averaged lidar
116 backscatter-to-extinction ratio (BER) was close to 0.024 sr⁻¹ (lidar ratio of ~41.7 sr), with a
117 large dispersion of ±33% over the whole observation period due to changing atmospheric
118 transport regimes and aerosol sources. The ground-based remote sensing measurements,
119 coupled with satellite observations, allowed to document i) dust particles up to 5 km (above
120 sea level) in altitude originating from Morocco and Algeria from 15 to 18 June with a peak in
121 aerosol optical thickness (AOT) of 0.25±0.05 at 355 nm, ii) a long-range transport of biomass
122 burning aerosol (AOT = 0.18±0.16) related to North American forest fires detected from 26 to
123 28 June, 2013 by the lidar between 2 and 7 km and iii) mixture of local sources including
124 marine aerosol particles and pollution from Spain. During the biomass burning event, the high
125 value of the particle depolarization ratio (8-14%) may imply the presence of dust-like
126 particles mixed with the biomass burning aerosols in the mid troposphere. **For the field**

127 | campaign period, we also show linearity with SEVIRI retrievals of the aerosol optical
128 | thickness despite 35% relative bias, which is discussed as a function of aerosol type.

129 | **1. Introduction**

130 | The Mediterranean has been identified as one of the "hot-spots" in projections of future
131 | climate change (Giorgi and Lionello, 2008) and it has been recently shown that aerosol direct
132 | and semi-direct effects, which were not properly taken into account in global climate change
133 | simulations (IPCC, 2014), have a significant impact on surface temperature, evaporation, and
134 | precipitation at the regional scale (Nabat et al., 2015), i.e. a likely positive feedback on the
135 | trend for future dryer and thus more turbid Mediterranean summers. Due to the variability of
136 | aerosol properties over the Mediterranean basin, this calls for a more representative
137 | description of aerosol optical properties and spatiotemporal distribution by both observations
138 | and models.

139 | Regional experiments including measurements of the vertical distribution of aerosols were
140 | performed some time ago to characterize aerosols over the Mediterranean Sea (i) in the
141 | framework of the MEDiterranean DUSt Experiment (MEDUSE) in 1997 (Hamonou et al.,
142 | 1999), (ii) the Scientific Training and Access to Aircraft for Atmospheric Research
143 | Throughout Europe (STAAARTE) airborne flights in 1997 (Dulac and Chazette, 2003) and
144 | 1998 (Formenti et al., 2002), (iii) with a lidar deployed in Crete (Gobbi et al., 2000) or an
145 | instrumented ultralight aircraft in Lampedusa (Di Iorio et al., 2003) during the Photochemical
146 | Activity and Ultraviolet Radiation (PAUR II) campaign in 1999, (iv) over the eastern
147 | Mediterranean basin during the Mediterranean Intensive Oxidant Study (MINOS; Lelieveld et
148 | al., 2002;) and Mediterranean Israeli Dust Experiment (MEIDEX; Levin et al., 2005) in 2001;
149 | and (v) over the urban and industrial region of Marseille-Fos-Berre on the French
150 | Mediterranean coast also in 2001 (Cros et al., 2004; Cachier et al., 2005) ; (vi) in the
151 | framework of the EARLINET network (Papayannis et al., 2008). Such past experiments have

152 produced very useful information about the vertical distribution of Mediterranean aerosol
153 optical properties, based on in-situ observations and lidar measurements. During those
154 preceding campaigns in the Mediterranean region, the use of aerosol lidars was focused on
155 rather short time periods, but they appear as a very powerful tool to identify the wide
156 spectrum of aerosol types encountered in the tropospheric column (e.g. Chazette, 2003;
157 Chazette et al., 2005a; Berthier et al., 2006; Groß et al., 2011; Tesche et al., 2011; Nisantzi et
158 al., 2014). The multidisciplinary programme Mediterranean Integrated Studies at the Regional
159 and Local Scales (MISTRALS; <http://www.mistrals-home.org>), initiated by CNRS/INSU in
160 2010 to study the future habitability of the Mediterranean region, offered the opportunity,
161 within the Chemistry-Aerosol Mediterranean Experiment (ChArMEx,
162 <http://charmex.lsce.ipsl.fr>), to conduct ground-based and airborne lidar observations at the
163 scale of the Western Mediterranean basin.

164 The ChArMEx/Aerosol Direct Radiative Effect in the Mediterranean (ADRMED) special
165 observation period (SOP-1a) was set-up from 11 June to 3 July to study aerosol optical
166 properties and radiative effects in the western Mediterranean during the dry season, which
167 shows a maximum in aerosol optical depth (Nabat et al., 2013). The campaign involved
168 several surface stations throughout the western Mediterranean, research aircrafts, and
169 instrumented balloons (Mallet et al., 2015). In this work, we focus on both active and passive
170 remote sensing observations performed at Menorca (Balearic Island, Spain) during this
171 campaign. The main goal of the paper is to demonstrate the benefit of continuous daytime and
172 nighttime lidar measurements during at least 3 weeks to derive aerosol optical properties. It
173 improves both the assessment of the diurnal variation of the aerosol distribution related to the
174 planetary boundary layer (PBL) growth and the probability to detect long range transports of
175 aerosol plumes. In section 2, we first present the experimental set-up. Retrieved aerosol
176 optical properties for both nighttime and daytime conditions are analysed in section 3 to give

177 an overall identification of aerosol types. In section 4, we discuss the different origins of
178 aerosol particles before discussing comparison with the Spinning Enhanced Visible and
179 InfraRed Imager (SEVIRI) retrievals and concluding in section 5.

180 **2. Ground-based remote sensing measurements**

181 During the campaign, our custom-made Raman lidar WALI (Chazette et al., 2014) was
182 operated together with an AERONET sunphotometer at Cap d'en Font
183 (http://aeronet.gsfc.nasa.gov/new_web/photo_db/Cap_d_En_Font.html) on the south-eastern
184 coast of the Balearic island of Menorca, Spain. The instruments were located within ~6 m
185 from each other, at 39°49'32.9"N, 04°12'29.3"E, at ~10 m above the mean sea level (amsl)
186 and less than 70 m from a small cliff on the sea shore. The choice to use only remote sensing
187 instruments is driven by the lack of representativeness of the ground-based in situ
188 measurements, which are mainly affected by local dynamical forcings. This is especially true
189 in coastal regions (Chazette, 2003). The selected location is mainly affected by Saharan and
190 Spanish air masses. **Figure 1** shows the location of the station approximately in the centre of
191 the western Mediterranean basin. The campaign average aerosol optical thickness (AOT_{550} , at
192 550 nm) distribution derived from SEVIRI on-board the geostationary Meteosat Second
193 Generation (MSG) platform is reported in this figure. It shows a classical North-South
194 decreasing gradient in the western Mediterranean Basin due to African dust with maximum
195 values between 0.20 and 0.25 in the Alboran Sea, and minimum values of ~0.12 in the Gulf of
196 Lyon. Intermediate values of ~0.17 are found around Menorca.

197 **2.1. Raman lidar**

198 The WALI instrument uses an emitted wavelength of 354.7 nm and is designed to fulfil
199 eye-safety conditions. The instrument, its calibration and the associated errors are documented
200 in Chazette et al. (2014) and will not be detailed here. During all the experiment, the
201 acquisition was performed continuously with a vertical resolution of 15 m for mean profiles

202 | of 1000 laser shots leading to a temporal sampling close to 1 min. The presence of clouds was
203 | visually detected in the lidar time series of range-corrected lidar backscattered profile and the
204 | corresponding periods were removed. Two validated (e.g. Dieudonné et al., 2015)
205 | measurement synergy types have been used to retrieve the aerosol optical properties from the
206 | lidar. During daytime the sunphotometer AOT_{355} is considered as a constraint for the lidar
207 | inversion as in Chazette (2003). Note that using the total AOT only allows us to retrieve a
208 | column-averaged or equivalent backscatter-to-extinction ratio (BER, product of the
209 | backscatter phase function and the single scattering albedo, inverse of the lidar ratio LR),
210 | integrating all the aerosol layers. During nighttime, the two elastic and the N_2 -Raman
211 | channels of the lidar are used to determine simultaneously the aerosol BER, the vertical
212 | profile of the aerosol extinction coefficient (α_e), and the linear particle depolarization ratio
213 | (PDR). All methodological details are well presented in Royer et al. (2011), Chazette et al.
214 | (2012a) and Chazette et al. (2014). The relative uncertainty on the BER is ~5% (resp. ~10%)
215 | during nighttime (resp. daytime). The relative uncertainties on the PDR are close to 10% for
216 | the encountered AOT at 355 nm ($AOT_{355} > 0.2$). The relative uncertainty on the AOT is less
217 | than 2%. The relative uncertainty on the water vapour mixing ratio (WVMR) is between 7
218 | and 11% within the first kilometres of the atmosphere.

Mis en forme : Français (France)

219 | Two representative examples of AOT and BER retrieval are given in Figure 2 corresponding
220 | to the main aerosol sources, biomass burning and desert dust observed during this campaign.
221 | They demonstrate the good agreement between the cumulative AOT derived from the N_2 -
222 | Raman and the elastic channels. The calculations have been performed using the average
223 | profile of nighttime measurements during the nights of 16-17 and 27-28 June, for biomass and
224 | dust cases, respectively. To improve the inversion, the mean profiles have been inverted using
225 | an altitude-variable BER and a regularization approach (Royer et al., 2011). For the first
226 | example, the BER (LR) is close to 0.04 sr^{-1} (25 sr) in the marine boundary layer (MBL) and

227 decreases with the altitude to reach values between 0.02 and 0.025 sr⁻¹ (50 and 40 sr) between
228 2 and 3 km amsl. The values of *BER* are similar for the second example in the MBL, but after
229 decreasing below 0.02 sr⁻¹ in the aerosol layer above the MBL, they significantly increase
230 above 4 km amsl to reach ~0.025 sr⁻¹. These two profiles correspond to the main contributions
231 of aerosol sources encountered during this period: maritime aerosol in the MBL
232 (BER ~ 0.04 sr⁻¹ or LR ~ 25 sr), dust (BER ~ 0.025 sr⁻¹ or LR ~ 40 sr) and biomass burning or
233 local pollution (BER < 0.02 sr⁻¹ or LR > 50 sr).

234 2.2. Sunphotometer

235 The Cimel[®] sunphotometer is part of the Aerosol Robotic Network (AERONET;
236 http://aeronet.gsfc.nasa.gov/cgi-bin/type_piece_of_map_opera_v2_new; Holben et al., 1998).
237 It performs measurements of solar light extinction at 8 wavelengths in the solar spectrum
238 between 340 and 1020 nm to retrieve the AOT at 7 wavelengths. The instrument field of view
239 is about 1° and the channel bandwidths are less than 20 nm. The instrument was calibrated
240 prior to and after the campaign by the observation service Photométrie pour le Traitement
241 Opérationnel de Normalisation Satellitaire (PHOTONS; <http://loaphotons.univ-lille1.fr/>), the
242 French component of AERONET. We have used Level-2 quality assured data. The AOT is
243 retrieved with a maximal absolute uncertainty of 0.02, independent of the aerosol load. The
244 aerosol optical thickness at the lidar wavelength of 355 nm (AOT_{355}) has been assessed using
245 the Ångström exponent (Ångström, 1964) and the sunphotometer AOT at 380 and 440 nm.
246 Sunphotometer AOT values at 500 and 675 nm are also used in this work for a better
247 comparison to satellite products described below. Additionally, these measurements were
248 checked against and completed by a SOLAR Light[®] Microtops II manual sunphotometer,
249 calibrated by PHOTONS shortly before the campaign (AERONET instrument #695). **The**
250 **AOT accuracy is similar to that of the automated Cimel sunphotometer. Nevertheless, manual**

251 solar targetting induces an additional bias which leads to an absolute uncertainty of the order
252 of 0.04 as compared to simultaneous measurements by an automated sunphotometer.

253 3. Temporal continuity of the aerosol optical properties

254 3.1. Vertically integrated aerosol optical properties derived from the sunphotometer

255 Both times series of AOT at 500 nm (AOT_{500}) and Ångström exponent between 440 and
256 675 nm, as directly measured by the sunphotometer, are plotted in Figure 3.

257 AOT and Ångström exponent both exhibit a strong variability due to the succession of aerosol
258 events of different types, as revealed by the large range of variation of the Ångström exponent
259 between ~0.4 and 2.15. The fine mode fraction of AOT also reported in the figure clearly co-
260 varies with the Ångström exponent. The coarse mode contribution is dominant from 16 to 20
261 June (coarse mode fraction of AOT between 50 and 80%) and also important on 24-25 June
262 (35 to 70%). The AOT appears to be higher with values larger than 0.2 during such periods.
263 The AOT, which is below 0.38 (on 18 June) during the first 2 weeks of campaign,
264 significantly increases on 26-28 June, showing several maxima (up to more than 0.6 on 27
265 June). Variations with particularly large amplitude appear on the 26 and 27 June. Usually
266 such peaks are due to North-African dust aerosol transport over the Western Mediterranean
267 basin (e.g. Moulin et al., 1998; Hamonou et al., 1999). In our case, the Ångström exponent
268 ranging between 1 and 1.6 appears too high to support the hypothesis a dominant presence of
269 dust particles. Values of the Ångström exponent over 1.5 are typical of pollution-like or
270 biomass burning aerosols (Chazette et al., 2005b) and an average value of 1.80 has been
271 observed for non-dust conditions over the Mediterranean by Paronis et al. (1998).
272 Computations by Hamonou et al. (1999) suggest that a dust contribution to this AOT cannot
273 be excluded but should be under a 0.45 fraction for the observed range of Ångström exponent.
274 The lowest AOT values observed on 10 June together with a low range of Ångström exponent
275 (0.01-0.21) are typical of a clear marine atmosphere with an aerosol population dominated by

276 sea-salt particles. We notice that the uncertainty on the Ångström exponent grows as the AOT
277 decreases. For AOT <0.15, the meaning of the Ångström exponent is subject to caution.

278 3.2. Aerosol optical properties derived from the ground-based lidar WALI

279 The temporal evolution of the BER derived from both the lidar measurements and the
280 sunphotometer are compared in [Figure 4](#). The sunphotometer-derived column-integrated BER
281 of the aerosols can be computed from the single scattering albedo and the phase function at a
282 scattering angle of 180° and 440 nm wavelength derived from the operational algorithm of
283 AERONET (Dubovik and King, 2000). The root mean square error (rmse in gray area) on the
284 lidar-derived BER, determined as the variability over 20 minutes, is close to 0.004 sr⁻¹ on
285 average, which is comparable with the one retrieved by Chazette et al. (2012b) with a similar
286 lidar system set-up in Menorca in the 2012 autumn season. We note a good coherence with
287 the BER at 440 nm derived by the AERONET sunphotometer. Yet, the sunphotometer-
288 derived BER seems to be underestimated by ~0.004 sr⁻¹ to 0.01 sr⁻¹ comparatively with the
289 lidar between 19 and 26 June; the larger variability bars at this period are due to a lighter
290 aerosol load (see [Figure 3](#)), which may explain part of this discrepancy. The higher values of
291 BER seen by the lidar would also be consistent with the hygroscopic properties of aerosols
292 within the PBL where the relative humidity significantly increases ([Figure 4b](#)) to reach more
293 than 90%. Indeed, BER may increase with the growth of aerosols. Moreover, the surface wind
294 speed rose on 26 June, with gusts reaching 12 m s⁻¹, which may seed the atmosphere with
295 marine aerosols (Blanchard et al., 1984).

296 For the sake of checking the consistency between the inversion procedures used during
297 nighttime and daytime, the histograms of the equivalent BER are compared in [Figure 5](#) for
298 daytime, nighttime, and the whole day. These histograms account for all lidar data inverted in
299 cloud-free conditions. The values greater than 0.045 sr⁻¹ are not significant and may represent
300 situations where the inversion process does not converge. Hence, ~10% of lidar profiles have

301 | not been considered in the synthesis. The nighttime BER distribution, with a BER value of
302 | $0.024 \pm 0.008 \text{ sr}^{-1}$, is only slightly smaller than the daytime distribution ($0.026 \pm 0.007 \text{ sr}^{-1}$).
303 | Hence, the BER values are deemed consistent between daytime and nighttime, and the
304 | synthesis on the entire experiment period shows an average of $0.024 \pm 0.008 \text{ sr}^{-1}$.

305 | The temporal evolutions of the vertical profile of aerosol extinction coefficient and PDR are
306 | shown in [Figure 6](#). PDR is an effective parameter to separate the contribution of the more
307 | spherical particles from the ones due to dust-like aerosols (e.g. Chazette et al., 2012b).
308 | Between 16 and 19 June the PDR value is between 10 and 27%, which is representative of
309 | non-spherical dust-like aerosols (Müller et al., 2007; Tesche et al., 2011) as identified in
310 | [Figure 4a](#) for *BER* between ~ 0.021 and 0.028 sr^{-1} . Except between 26 and 28 June, the aerosol
311 | content is dominated by spherical particles. Between 26 and 28 June a depolarizing layer is
312 | observed between ~ 5 and 7 km amsl . The PDR ranges between 8 and 14% suggesting that
313 | dust aerosols were mixed with other aerosol sources or were processed during their transport
314 | to Menorca. We will further discuss this case in section 4. When considering the temporal
315 | evolution of AOT also given in [Figure 6a](#), we note that lidar- and sunphotometer-derived
316 | AOT significantly differ on several occasions, especially in the cloudy periods (11, 20, 24, 25
317 | and 27 June). It is due to residual cloud layers in the lidar profiles, which are not seen on the
318 | line-of-sight of the sunphotometer, with a positive bias explained by the higher BER of these
319 | thin layers. In addition, from 26 to 28 June, the presence of high altitude aerosol layers also
320 | probably causes a strong heterogeneity of the aerosol BER in the tropospheric column (see
321 | [Figure 2b](#)), which may explain part of the previous discrepancies because the aerosol types
322 | may be very different against the altitude. This shows the limited relevance of the notion of
323 | column-equivalent BER in heterogeneous cases.

324 | 3.3. Evidence of contributions by aerosol type as discriminated by lidar

325 The temporal evolution of the observed aerosol species can be derived from the analysis of
326 the equivalent BER and PDR. Indeed, these two parameters, only calculated from the lidar
327 profiles, are sufficiently discriminating to identify the main aerosol types in most cases
328 (Burton et al., 2012). Three aerosol types are considered: i) dust-like aerosols with values of
329 BER and PDR centred on 0.022 sr^{-1} and 20%, respectively, ii) pollution aerosols with BER
330 and PDR centred on 0.015 sr^{-1} and 2%, respectively, and iii) marine aerosols with mean
331 values of BER and PDR centred on 0.04 sr^{-1} and 0%, respectively. For each aerosol type,
332 literature sometimes reports a large range of values, as shown in Tables 1 and 3 of Dieudonné
333 et al. (2015) for dust and pollution aerosols, respectively. These authors report at the same
334 wavelength BER from 0.013 to 0.026 sr^{-1} (resp. 0.011 to 0.017 sr^{-1}) and PDR from 13 to 25%
335 (resp. 3 to 5%) for pure dust or dusty mix (resp. pollution) aerosols. This range of values
336 includes the lidar observations performed by Groß et al. (2011) in Cape verde (off shore of
337 West Africa) with $BER = 0.017\text{-}0.020 \text{ sr}^{-1}$ ($PDR = 24\text{-}27\%$). The same authors report BER
338 from 0.042 to 0.053 sr^{-1} and PDR from 1 to 2% for marine aerosols. Figure 7 gives the
339 temporal evolution of the aerosol type after defining a specific colour map as a function of
340 BER and PDR. The lidar profiles were here averaged during 1 hour with a vertical resolution
341 of ~ 30 m. The aerosol backscatter coefficient (ABC) is coded by colour density: the more
342 saturated, the larger the ABC (white corresponds to $ABC = 0$). A specific colour scale is
343 affected to the couple of variables BER and PDR during nighttime. As the inversion using the
344 N_2 -Raman channel is not possible when the sun is up, the colour map has been only
345 associated with the PDR during daytime.

346 Such a graphic representation allows the refinement of the identification of the aerosol types
347 that are presented in Figure 4a. The higher BERs retrieved in Figure 4a between 19 and 26
348 June are due to a larger contribution of reflective aerosols in the lower layers, likely sea salt
349 particles, which may also be very hydrophilic. Pollution aerosols are present all along the

350 measurement period except during the dust event between 16 and 19 June. It is more difficult
351 to attribute the layer above 5 km amsl during the night of 26-27 June to a single aerosol
352 source because depolarization is observed simultaneously with low BER. This layer arrives
353 above a layer of biomass burning or polluted aerosols which spread between ~3 and 5 km
354 amsl. A succession of pollution plumes originated from different locations along the Spanish
355 coast contributes to the aerosol pollution load in the lower free troposphere over Menorca
356 according to the air mass trajectories (not shown). The intermittent plumes, lifted as the PBL
357 develops over Spain each afternoon, explain the periodic behavior observed in Figure 4a for
358 the temporal evolution of the column-equivalent BER. However for the 26-27 June period the
359 long range transport, revealed by the backtrajectories discussed hereafter, also shows a link
360 with the North American biomass burning aerosol sources. Note that long range transport of
361 biomass burning aerosols has always demonstrated to be a significant aerosol source over
362 Europe (e.g. Fiebig et al., 2003; Müller et al., 2005). This temporal evolution of aerosol types
363 based on the unique analysis of the lidar data is quite consistent with the column-integrated
364 observations of the AERONET sunphotometer, as discussed in section 3.1 and reported in
365 Figure 3.

366 3.4. Regional representativeness as seen by spaceborne measurements

367 The observations conducted from the Menorca Island station are relevant to the local
368 atmospheric column. In the following we put them in a more regional context using the
369 measurements performed by SEVIRI (e.g. Bennouna et al., 2009) and the spaceborne
370 instruments Moderate Resolution Imaging Spectroradiometers (MODIS; Salmonson et al.,
371 1989; King et al., 1992; <http://modis.gsfc.nasa.gov>). The MODIS data above land (few data
372 are available above sea due to sun-glitter) and the SEVIRI data above sea are combined in a
373 single map to check the reliability in terms of continuity between sea and continent.

374 The spatial resolution of the MYD04_L2 product of MODIS is $10 \times 10 \text{ km}^2$ at nadir. The
375 predicted uncertainty on the AOT at 550 nm over land is $\pm 0.15 \cdot AOT \pm 0.05$. The spatial
376 and temporal resolutions of SEVIRI measurements are $10 \times 10 \text{ km}^2$ and 15 minutes,
377 respectively. The uncertainty on the SEVIRI-derived AOT is very dependent on the aerosol
378 type (Bennouna et al., 2009). Compared to AERONET products from coastal stations,
379 Thieuleux et al. (2005) do not highlight any significant bias on the AOT at 550 nm derived
380 from SEVIRI for values between ~ 0.07 and 1. Their comparison based on observations in
381 2003 indicates that the SEVIRI AOT product is of somewhat lower quality at the
382 sunphotometer sites directly affected by a desert dust plume from northern Africa. This is
383 attributed to the fact that the aerosol models used to compute the look-up table does not
384 include a specific desert dust model. Bréon et al. (2011) report a bias of 0.07 from their more
385 exhaustive evaluation with AERONET sunphotometers over the period from June 2005 to
386 December 2010. From a similar linear fitting between MODIS and AERONET, they found a
387 smaller bias of ~ 0.02 and a correlation slope close to 1.

388 **Figure 8** shows the inter-comparison between quarter-hourly products from SEVIRI and from
389 the coincident AERONET sunphotometer of Menorca, including the AOT at 550 nm (**Figure**
390 **8a**) and the Ångström exponent (**Figure 8b**, computed between 630 and 810 nm, and 675 and
391 870 nm for SEVIRI and the sunphotometer, respectively). For the AOT, a linear least square
392 fit highlights a significant deviation from the 1:1 relationship with a factor of 0.65. The
393 additive bias is low, positive and close to 0.03. The mean rmse is ~ 0.066 . The main
394 discrepancies are mostly observed for the highest AOTs, occurring between 17-19 and 26-28
395 June when marine and dust aerosol are mixed and when biomass burning aerosols arrived
396 above the site. The latter case is likely also associated with aerosol mixing. The discrepancies
397 can be due to the resulting difficulty of the inversion process to identify a proper aerosol
398 model, even for dust particles which never completely prevail in terms of AOT. We note the

399 larger dispersions for the mixing of marine particles with dust or pollution aerosols. In the
400 following, we have corrected by -35% the SEVIRI AOT_{550} product. Whereas the
401 sunphotometer-derived Ångström exponent seems coherent with our previous classification,
402 our results suggest that the SEVIRI Ångström exponent product (Figure 8b) relatively large
403 discrepancies at all AOT (although less at larger values), mostly related to aerosol type, and
404 this microphysical properties. The dispersion is lower for the dust (red in the figure) and
405 biomass burning (brown in the figure) events, but with overestimation and underestimation,
406 respectively. Consequently, the SEVIRI-derived AOT_{550} product over ocean, that relies on the
407 evaluated Ångström exponent, should be carefully checked before use. **Note that these**
408 **conclusions on both AOT and Ångström exponent cannot be generalized to other areas or**
409 **other time periods without further investigation.**

410 The situations with the strongest AOT contrasts above the western Mediterranean basin are
411 shown in Figure 9. We can notice the very good continuity, after the correction of the
412 SEVIRI-derived AOT, between sea and continent (MODIS-derived AOT). The main aerosol
413 events are linked with either the highest PDR observed between 16 and 19 June, or the highest
414 altitude transport (above 5 km amsl) between 26 and 28 June. The first event is due to desert
415 dust aerosols off the Moroccan and Algerian coasts (see also Figure 4). The second event
416 reveals a plume crossing the Mediterranean from North to South and will be discussed
417 hereafter. It is associated with a decrease of the BER after 26 June as shown in Figure 4a after
418 26 June.

419 **4. Discussion**

420 The pollution transport events observed at Menorca in the first part of the campaign, 12-18
421 June (Figure 4), are associated with the lowest values of the BER. To investigate their origins,
422 we ran the HYbrid Single-Particle Lagrangian Integrated Trajectory (HYSPLIT) model
423 (Draxler and Rolph, 2014) with 3-hourly archived meteorological data provided by the US

424 National Center for Environmental Prediction (NCEP) Global Data Assimilation System
425 (GDAS) at the horizontal resolution of 0.5° . Two-day back-trajectories (not shown) clearly
426 trace those polluted air masses back to Spain. Still in the same period, we note an increase of
427 the BER during nighttime. It may be due to a higher relative contribution of hygroscopic
428 aerosols below 1 km amsl as explained in section 3. Between 18 and 26 June (Figure 4), the
429 BER reaches $\sim 0.04 \text{ sr}^{-1}$ ($LR = 25 \text{ sr}$) as observed by Flamant et al. (2000) for marine aerosols
430 over the open ocean. Nevertheless, we also note weak-medium surface wind speeds between 2
431 and 8 m s^{-1} not favourable to a strong contribution of sea salt particles in the lower
432 troposphere.

433 Satellite data show the arrival of an African dust plume from the Alboran Sea over the
434 Balearic Islands starting slowly on 15 June and leaving Menorca on 19 June. The AOT
435 slightly increases from 16 to 18 June, when the densest part of the dust plume passes over the
436 Menorca Island, to reach $AOT_{355} = 0.25 \pm 0.05$. As highlighted by 3-day back-trajectories (not
437 shown), the dust plume came from Morocco and Algeria, as also illustrated by the satellite
438 image in Figure 9a. Moreover, measurements of the Cloud-Aerosol Lidar with Orthogonal
439 Polarization (CALIOP, PC-SCI-202.03, Vaughan et al., 2004) on 16 June highlight dust
440 aerosols below 37.3° of latitude and polluted-dust aerosols above this latitude, which confirm
441 the classification given in Figure 7. In the dust layer above 1 km amsl, the PDR is $20 \pm 5\%$ and
442 the mean BER (LR) is $0.024 \pm 0.002 \text{ sr}^{-1}$ ($\sim 41.7 \pm 4 \text{ sr}$). Note that, as shown Figure 2a and
443 previously discussed, the BER significantly evolves within the low and medium troposphere
444 from 0.04 sr^{-1} ($LR = 25 \text{ sr}$) in the MBL to $\sim 0.020\text{-}0.025 \text{ sr}^{-1}$ ($LR \sim 50\text{-}40 \text{ sr}$) in the dust layer
445 situated above $\sim 2 \text{ km amsl}$. A relative peak is observed in the BER profile between 1 and
446 2 km amsl associated with smaller values of the aerosol extinction coefficient (Figure 6). This
447 intermediate layer is associated with $PDR < 2\%$ and may be mainly affected by both marine
448 and pollution aerosols.

449 The high-altitude aerosol event observed between 4 and 7 km amsl above the western
450 Mediterranean basin from 26 to 28 June is not usual in its nature since it results from a very
451 turbid plume ($AOT_{550} > 0.6$) arriving from the NE Atlantic as visible on the Bay of Biscay on
452 26 June in **Figure 10**. Formenti et al. (2002) have already documented with airborne
453 measurements such an occurrence of 10-day aged haze layers from Canadian fires over the
454 eastern Mediterranean in August 1998. Seven days-back trajectories have been computed with
455 the HYSPLIT model (**Figure 10**). The back trajectories are superimposed on a MODIS AOT
456 image combining data from 24 June, 2013. Dense aerosol plumes appear all along a transport
457 pathway over the Northern Atlantic, with a dark red colour associated with AOT_{550} values
458 larger than 1. Note that the AOT even reaches 5 for many pixels, maybe because cloud
459 contribution is also included as can be seen in the true colour image available on
460 <https://earthdata.nasa.gov/labs/worldview/>. As shown in **Figure 10**, the biomass burning
461 plume observed at 6 km over Menorca on 27 June crossed the Atlantic Ocean at altitudes
462 between 4 and 8 km amsl. The plume is associated with forest burning **occurring in Canada**
463 **and Colorado**.

464 The possible source regions are discussed in detail in the companion paper of Ancellet et al.
465 (2016). It includes contributions from two different plumes: biomass burning aerosol from
466 North America and dust transported westward over the Atlantic by the trade winds.
467 Trajectories from the other plume detected close to 4 km amsl over Menorca by the lidar on
468 28 June (**Figure 6**) also come from North America with little contribution from the Atlantic
469 Saharan dust. The North American aerosol event of 26-27 June is characterized by
470 $AOT_{355} = 0.18 \pm 0.16$ above Menorca. It represents ~50% of the total columnar AOT
471 ($AOT_{355} = 0.41 \pm 0.12$) encountered during this day. It is associated with a moister air mass,
472 with a WVMR close to 1-2 g/kg, comparatively to the clean free mid-troposphere (0.5 g/kg),
473 as derived from the H₂O-Raman lidar channel. The uplifting of air masses from the lower

474 troposphere occurs either above the continental US or above the Atlantic ocean as discussed
475 in Ancellet et al. (2016). The equivalent *BER* has been assessed to be $0.023\pm 0.002\text{ sr}^{-1}$
476 ($LR \sim 43.5\pm 4\text{ sr}$) and corresponds about to the mean value of the vertical profile of *BER*
477 given in Figure 2b. As previously, the value retrieved in the MBL correspond to marine
478 aerosols. The *BER* in the mixture of biomass burning aerosol and dust is determined as
479 $0.025\pm 0.002\text{ sr}^{-1}$ ($LR \sim 40\pm 3\text{ sr}$) with a PDR between 8 and 14%. PDR values between 8%
480 and 18% were measured over Cyprus by the lidar of Limassol (Nisantzi et al., 2014) for
481 almost fresh biomass burning aerosols mixed with dust-like particles uplifted by thermal
482 convection and transported above the lidar site. However, the dust observed over Cyprus
483 presents a larger *BER* than the one generally derived over Sahara. Groß et al. (2011) also
484 report larger values of PDR (18-22%) for a mixture of biomass burning and Saharan dust
485 aerosol over Cape Verde with *BER* between 0.014 and 0.016 sr^{-1} (LR between 60 and 70 sr).
486 In our case, the aerosols are more aged (at least 7 days) and may be more spherical due to
487 water vapour condensation during transport over the Atlantic Ocean. We note cloud formation
488 along some filaments created from the initial plume (not shown). Such a phenomenon
489 decreases the PDR. Nevertheless, the value of PDR is higher and may indicate the presence of
490 dust-like particles within the biomass burning plume. The high vertical resolution of the
491 CALIOP lidar (30-60 m) can be processed to derive aerosol type and optical properties of the
492 aerosol layers (e.g. Vaughan et al., 2004; Thomason et al., 2007; Kim et al., 2008; Berthier et
493 al., 2006) as the PDR. The 8-14% PDR measured at 355 nm by the WALI lidar appears
494 comparable to the 10% PDR at 532 nm observed by CALIOP (the ground track is given in
495 Figure 9d) off the Mediterranean Spanish coast at 1°E in a layer between 38°N and 39°N on
496 28 June, 0200 UTC (see Ancellet et al. 2016 in the same issue). Over the Atlantic Ocean (24
497 June), the aerosol plume is identified by CALIOP measurements either of smoke type or of
498 polluted dust type.

499 **5. Conclusion**

500 Aerosol optical properties in the tropospheric column were derived from the measurements
501 performed continuously, during three weeks in June and early July 2013, at Menorca Island
502 during the Chemistry-Aerosol Mediterranean Experiment / Aerosol Direct Radiative Effect in
503 the Mediterranean (ChArME_x/ADRIMED) special observation period (SOP-1a). The
504 measurements sampled air masses with very different aerosol content and a large range of
505 optical thicknesses ($AOT_{355} = 0.29 \pm 0.17$), which has been shown as representative of the
506 years 2011 to 2013 ($AOT_{355} = 0.24 \pm 0.15$). There are only a few cases where the aerosol layers
507 are not composed of a mixture of different aerosol types. They are originating from the
508 surrounding sea, the Spanish coastal cities, the North Africa deserts and even distant forest
509 fires in North America. We have noted that the complex mixing of aerosols likely impact the
510 retrieval of the AOT from SEVIRI leading to a relative bias close to 35%.

511 The instrumental synergy, coupling either the sunphotometer or the N₂-Raman channel with
512 the elastic channel, allows a well-constrained processing of the lidar measurements, from
513 which we were able to follow the evolution of the aerosol optical properties between night
514 and day. In particular, the continuity of column-equivalent BER measurements is ensured.
515 Lidar observations allowed locating scattering layers in the troposphere, and in particular
516 identifying a complex aerosol transport from North America in the middle troposphere
517 (between 2 and 7 km amsl). Air masses took between 5 and 7 days to arrive over the
518 Mediterranean Sea. There has been a great variability in the nature of aerosols in the
519 troposphere during this period from 26 to 28 June, 2013. This variability is evidenced by the
520 BER profile estimated from the Raman lidar WALI, with a strong variance ($BER(LR)$
521 $= 0.024 \pm 0.008 \text{ sr}^{-1}$ ($\sim 41.7 \pm 14 \text{ sr}$), above 4 km amsl and $< 0.02 \text{ sr}^{-1}$ ($> 50 \text{ sr}$) between 2 and
522 4 km amsl). However, such variability has weak impact on the AOT measurements, be it
523 | during nighttime or daytime. We have also observed the presence of depolarizing particles

524 (*PDR* ~8-14% @355 nm) in a biomass burning plume originating from North America
525 corresponding to Saharan dust re-circulated over the Atlantic Ocean, as discussed in the
526 companion paper by Ancellet et al. (2016).

527 These results show that an assessment of the radiative budget of aerosols over the western
528 Mediterranean basin can be easily performed by considering the average optical properties of
529 the particles. Nevertheless, for the evaluation of atmospheric heating rates and possible
530 associated effects on cloud formation, account must be taken of the single scattering albedo,
531 which is linked to the vertical evolution of the aerosol types given by our classification.
532 Moreover, the single scattering albedo may be constrained by the lidar-derived BER as in
533 Randriamiarisoa et al. (2004) or Raut and Chazette (2008). The latter has indeed been shown
534 in this campaign to be very variable, both in time and altitude, due to the mixing of very
535 different aerosol contributions over the Mediterranean Sea.

536 **Acknowledgements.** This work was supported by the French space agency (CNES) and the
537 Commissariat à l'Énergie Atomique (CEA). The campaign at Menorca was also supported by
538 CNRS/INSU and Météo-France through the MISTRALS/ChArMEx programme, and by the
539 Spanish Ministry of Science and Innovation and FEDER funds under the projects TEC2012-
540 34575, UNPC10-4E-442 and CGL2011-13580-E/CLI. Matthieu Jeannot from LPC2E,
541 François Dulac and Sahar Hassanzadeh from LSCE are acknowledged for their technical help
542 during the campaign. Juan Ramon Moreta Gonzalez and Miguel Angel Heredia Jodar from
543 AEMET are acknowledged for AERONET data from Palma.

544 6. References

545 Ancellet, A., Pelon, J., Totems, J., Chazette, P., Bazureau, A., Sicard, M., Di Iorio, T., Dulac,
546 M., and Mallet, M.: Long range transport and mixing of aerosol sources during the 2013
547 North American biomass burning episode : analysis of multiple lidar observations in the
548 Western Mediterranean basin, *accepted to Atmos. Chem. Phys.*, this special issue, 2016.

- 549 Ångström, A.: The parameters of atmospheric turbidity, *Tellus*, 16, 64-75, 1964.
- 550 Bennouna, Y. S., de Leeuw, G., Piazzola, J., and Kurmierczyk-Michulec, J.: Aerosol remote
551 sensing over the ocean using MSG-SEVIRI visible images, *J. Geophys. Res.*, 114, *D23203*,
552 doi: 10.1029/2008JD011615, 2009.
- 553 Berthier, S., Chazette, P., Couvert, P., Pelon, J., Dulac, F., Thieuleux, F., Moulin, C., and
554 Pain, T. : Desert dust aerosol columnar properties over ocean and continental Africa from
555 Lidar in-Space Technology Experiment (LITE) and Meteosat synergy, *J. Geophys. Res.*, 111,
556 D21202, doi:10.1029/2005JD006999, 2006.
- 557 Blanchard, C.D., Woodcock, A.H., and Cipriano, R.J., The Vertical Distribution of
558 Concentration of Sea Salt in the Marine Atmosphere near Hawaii, *Tellus*, 36B, 118-125,
559 1984.
- 560 Bréon, F.-M. M., Vermeulen, A., and Descloitres, J.: An evaluation of satellite aerosol
561 products against sunphotometer measurements, *Remote Sens. Environ.*, 115(12), 3102–3111,
562 doi:10.1016/j.rse.2011.06.017, 2011.
- 563 Burton, S. P., Ferrare, R. A., Hostetler, C. A., Hair, J. W., Rogers, R. R., Obland, C. F.,
564 Butler, M. D., Cook, A. L., Harper, D. B., and Froyd, K. D.: Aerosol classification using
565 airborne High Spectral Resolution Lidar measurements—methodology and examples *Atmos.*
566 *Meas. Technol.*, 5, 73–98, 2012.
- 567 Cachier, H., Aulagnier, F., Sarda, R., Gautier, F., Masclet, P., Besombes, J.-L., Marchand, N.,
568 Despiiau, S., Croci, D., Mallet, M., Laj, P., Marinoni, A., Deveau, P.-A., Roger, J.-C., Putaud,
569 J.-P., Van Dingenen, R., Dell'Acqua, A., Viidanoja, J., Martins-Dos Santos, S., Liouise, C.,
570 Cousin, F., Rosset, R., Gardrat, E., and Galy-Lacaux, C.: Aerosol studies during the
571 ESCOMPTE experiment: An overview, *Atmos. Res.*, 74, 547–563, 2005.
- 572 Chazette, P.: The monsoon aerosol extinction properties at Goa during INDOEX as measured
573 with lidar, *J. Geophys. Res.*, 108(D6), 4187, doi:10.1029/2002JD002074, 2003.
- 574 Chazette, P., Couvert, P., Randriamiarisoa, H., Sanak, J., Bonsang, B., Moral, P., Berthier, S.,
575 Salanave, S., and Toussaint, F.: Three-dimensional survey of pollution during winter in French
576 Alps valleys, *Atmos. Environ.*, 39, 1035-1047, 2005a.
- 577 Chazette, P., Randriamiarisoa, H., Sanak, J., Couvert, P., and Flamant, C.: Optical properties
578 of urban aerosol from airborne and ground-based in situ measurements performed during the
579 Etude et Simulation de la Qualité de l'air en Ile de France (ESQUIF) program, *J. Geophys.*
580 *Res.*, 110(D2), D02206, doi:10.1029/2004JD004810, 2005b.
- 581 Chazette, P., Dabas, a., Sanak, J., Lardier, M. and Royer, P.: French airborne lidar
582 measurements for Eyjafjallajökull ash plume survey, *Atmos. Chem. Phys.*, 12(15), 7059–
583 7072, doi:10.5194/acp-12-7059-2012, 2012a.
- 584 Chazette, P., Bocquet, M., Royer, P., Winiarek, V., Raut, J. C., Labazuy, P., Gouhier, M.,
585 Lardier, M., and Cariou, J. P.: Eyjafjallajökull ash concentrations derived from both lidar and
586 modeling, *J. Geophys. Res. Atmos.*, 117, D00U14, doi:10.1029/2011JD015755, 2012b.

587 Chazette, P., Marnas, F., and Totems, J.: The mobile Water vapor Aerosol Raman Lidar and
588 its implication in the framework of the HyMeX and ChArMEX programs: application to a dust
589 transport process, *Atmos. Meas. Tech.*, 7(6), 1629–1647, doi:10.5194/amt-7-1629-2014,
590 2014.

591 Cros, B., Durand, P., Cachier, H., Drobinski, Ph., Fréjafon, E., Kottmeier, C., Perros, P.,
592 Peuch, V., Ponche, J.-L., Robin, D., Said, F., Toupance, G., and Wotham, H.: The
593 ESCOMPTE Program: an overview, *Atmos. Res.*, 69, 241–279, 2004.

594 Dieudonné, E., Chazette, P., Marnas, F., Totems, J., and Shang, X.: Lidar profiling of aerosol
595 optical properties from Paris to Lake Baikal (Siberia), *Atmos. Chem. Phys.*, 15(9), 5007–
596 5026, doi:doi:10.5194/acp-15-5007-2015, 2015.

597 Draxler, R. R. R. and Rolph, G. D. D.: HYSPLIT (HYbrid Single-Particle Lagrangian
598 Integrated Trajectory) Model access via NOAA ARL READY Website, available at:
599 <http://www.arl.noaa.gov/HYSPLIT.php> (last access: november 2015). NOAA Air Resources
600 Laboratory, College Park, MD, 2014.

601 Di Iorio, T., di Sarra, A., Junkermann, W., Cacciani, M., Fiocco, G., and Fuà, D.:
602 Tropospheric aerosols in the Mediterranean: 1. Microphysical and optical properties, *J.*
603 *Geophys. Res.*, 108, D02201, doi: 10.1029/2002JD002815, 2003.

604 [Dubovik, O. and King, M. D.: A flexible inversion algorithm for retrieval of aerosol optical](#)
605 [properties from Sun and sky radiance measurements, *J. Geophys. Res. Atmos.*, 105\(D16\),](#)
606 [20673–20696, doi:10.1029/2000JD900282, 2000.](#)

Mis en forme : Anglais (États Unis)

Mis en forme : Justifié

607 Dulac, F., and Chazette, P.: Airborne study of a multi-layer aerosol structure in the eastern
608 Mediterranean observed with the airborne polarized lidar ALEX during a STAAARTE
609 campaign (7 June 1997), *Atmos. Chem. Phys.*, 3, 1817–1831, doi:10.5194/acp-3-1817-2003,
610 2003.

611 Flamant, C., Pelon, J., Chazette, P., Trouillet, V., Quinn, P. K., Frouin, R., Bruneau, D.,
612 Francois Leon, J., Bates, T. S., Johnson, J., and Livingston, J.: Airborne lidar measurements
613 of aerosol spatial distribution and optical properties over the Atlantic Ocean during a
614 European pollution outbreak of ACE-2, *Tellus B*, 52(2), 662–677, doi:10.1034/j.1600-
615 0889.2000.00083.x, 2000.

Mis en forme : Anglais (États Unis)

616 Fiebig, M., Stohl, A., Wendisch, M., Eckhardt, S. and Petzold, A.: Dependence of solar
617 radiative forcing of forest fire aerosol on ageing and state of mixture, *Atmos. Chem. Phys.*,
618 3(3), 881–891, doi:10.5194/acp-3-881-2003, 2003.

Mis en forme : Police :(Par défaut)
Times New Roman, (asiatique) +Corps
asiatique (SimSun), 12 pt, Anglais
(États Unis)

619 Formenti, P., Boucher, O., Reiner, T., Sprung, D., Andreae, M. A., Wendisch, M., Wex, H.,
620 Kindred, D., Tzortziou, M., Vasaras, A., and Zerefos, C.: STAAARTE-MED 1998 summer
621 airborne measurements over the Aegean Sea. 2. Aerosol scattering and absorption, and
622 radiative calculations, *J. Geophys. Res.*, 107, 4451, doi:10.1029/2001JD001536, 2002.

623 Giorgi, F. and Lionello, P.: Climate change projections for the Mediterranean region, *Glob.*
624 *Planet. Change*, 63(2-3), 90–104, doi:10.1016/j.gloplacha.2007.09.005, 2008.

- 625 Gobbi, G.P., Barnaba, F., Blumthaler, M., Labow, G., and Herman, J.L.: Observed effects of
626 particles nonsphericity on the retrieval of marine and desert dust aerosol optical depth by
627 lidar, *Atmos. Res.*, 61, 1-14, 2000.
- 628 Groß, S., Tesche, M., Freudenthaler, Toledano, C., V., Wiegner, Ansmann, A., Althausen, D.,
629 and Seefeldner, M.: Characterization of Saharan dust, marine aerosols and mixtures of
630 biomass-burning aerosols and dust by means of multi-wavelength depolarization and Raman
631 lidar measurements during SAMUM 2, *Tellus*, 63B, 706-724, 2011.
- 632 Hamonou, E., Chazette, P., Balis, D., Dulac, F., Schneider, X., Galani, E., Ancellet, G. and
633 Papayannis, A.: Characterization of the vertical structure of Saharan dust export to the
634 Mediterranean basin, *J. Geophys. Res.*, 104(D18), 22257, doi:10.1029/1999JD900257, 1999.
- 635 Holben, B. N., Eck, T. F., Slutsker, I., Tanré, D., Buis, J. P., Setzer, A., Vermote, E. F.,
636 Reagan, J. A., Kaufman, Y. J., Nakajima, T., Lavenu, F., Jankowiak, I., and Smirnov, A.:
637 AERONET – A federated instrument network and data archive for aerosol characterization,
638 *Remote Sens. Environ.*, 66, 1–16, 1998.
- 639 IPCC, 2014: Climate Change 2014: Impacts, Adaptation, and Vulnerability. Part A: Global
640 and Sectoral Aspects. Contribution of Working Group II to the Fifth Assessment Report of the
641 Intergovernmental Panel on Climate Change, Field, C.B., Barros, V.R., Dokken, D.J., Mach,
642 K.J., Mastrandrea, M.D., Bilir, T.E., Chatterjee, M., Ebi, K.L., Estrada, Y.O., Genova, R.C.,
643 Girma, B., Kissel, E.S., Levy, A.N., MacCracken, S., Mastrandrea, P.R., and White, L.L.
644 (eds), Cambridge University Press, Cambridge, United Kingdom and New York, NY, USA,
645 1132 pp.
- 646 Kim, S. W., Berthier, S., Raut, J.-C., Chazette, P., Dulac, F., and Yoon, S.-C.: Validation of
647 aerosol and cloud layer structures from the space-borne lidar CALIOP using a ground-based
648 lidar in Seoul, Korea, *Atmos. Chem. Phys.*, 8, 3705–3720, doi:10.5194/acp-8-3705-2008,
649 2008.
- 650 King, M. D., Kaufman, Y. J., Menzel, P. and Tanré, D.: Remote-sensing of cloud, aerosol,
651 and water-vapor properties from the Moderate Resolution Imaging Spectroradiometer
652 (MODIS), *IEEE Trans. Geosci. Remote Sensing*, 30, 2-27, 1992.
- 653 Klett, J. D.: Lidar inversion with variable backscatter/extinction ratios, *Appl. Opt.*, 24(11),
654 1638, doi:10.1364/AO.24.001638, 1985.
- 655 Lelieveld, J., Berresheim, H., Borrmann, S., Crutzen, P.J., Dentener, F.J., Fischer, H.,
656 Feichter, J., Flatau, P.J., Heland, J., Holzinger, R., Korrman, R., Lawrence, M.G., Levin, Z.,
657 Markowicz, K.M., Mihalopoulos, N., Minikin, A., Ramanathan, V., de Reus, M., Roelofs,
658 G.J., Scheeren, H.A., Sciare, J., Schlager, H., Schultz, M., Siegmund, P., Steil, B., Stephanou,
659 E.G., Stier, P., Traub, M., Warneke, C., Williams, J., and Ziereis, H.: Global air pollution
660 crossroads over the Mediterranean, *Science*, 298, 794–799, 2002.
- 661 Levin, Z., Teller, A., and Ganor, E.: On the interactions of mineral dust, sea-salt particles, and
662 clouds: A measurement and modeling study from the Mediterranean Israeli Dust Experiment
663 campaign, *J. Geophys. Res.*, 110, D05207, doi: 10.1029/2005JD005810, 2005.

664 Mallet, M., et al.: Overview of the Chemistry-Aerosol Mediterranean Experiment/Aerosol
665 Direct Radiative Forcing on the Mediterranean Climate (ChArMEx/ADRIMED) summer
666 2013 campaign, *Atmos. Chem. Phys.*, this special issue, 2015.

667 Moulin C., Lambert, C. E., Dayan, U., Masson, V., Ramonet, M., Bousquet, P., Legrand, M.,
668 Balkanski, Y. J., Guelle, W., Marticorena, B., Bergametti, G., and Dulac, F.: Satellite
669 climatology of African dust transport in the Mediterranean atmosphere, *J. Geophys. Res.*, 103,
670 13137–13144, 1998.

671 Müller, D., Mattis, I., Ansmann, A., Wandinger, U., Ritter, C. and Kaiser, D.: Raman lidar
672 observations of aged Siberian and Canadian forest fire smoke in the free troposphere over
673 Germany in 2003: Microphysical particle characterization, *J. Geophys. Res.*, 110(D17),
674 D17201, doi:10.1029/2004JD005756, 2005.

675 Müller, D., Ansmann, A., Mattis, I., Tesche, M., Wandinger, U., Althausen, D., and Pisani,
676 G.: Aerosol-type-dependent lidar ratios observed with Raman lidar, *J. Geophys. Res. Atmos.*,
677 112, D16202, doi:10.1029/2006JD008292, 2007.

678 Nabat, P., Somot, S., Mallet, M., Chiapello, I., Morcrette, J. J., Solmon, F., Szopa, S., Dulac,
679 F., Collins, W., Ghan, S., Horowitz, L. W., Lamarque, J. F., Lee, Y. H., Naik, V., Nagashima,
680 T., Shindell, D. and Skeie, R.: A 4-D climatology (1979–2009) of the monthly tropospheric
681 aerosol optical depth distribution over the Mediterranean region from a comparative
682 evaluation and blending of remote sensing and model products, *Atmos. Meas. Tech.*, 6, 1287–
683 1314, doi:10.5194/amt-6-1287-2013, 2013.

684 Nabat, P., Somot, S., Mallet, M., Michou, M., Sevault, F., Driouech, F., Meloni, D., Di Sarra,
685 A., Di Biagio, C., Formenti, P., Sicard, M., Léon, J.-F., and M.-N. Bouin: Dust aerosol
686 radiative effects during summer 2012 simulated with a coupled regional aerosol–atmosphere–
687 ocean model over the Mediterranean, *Atmos. Chem. Phys.*, 15, 3303–3326, doi: 10.5194/acp-
688 15-3303-201, 2015.

689 Nisantzi, A., Mamouri, R. E., Ansmann, A., and Hadjimitsis, D.: Injection of mineral dust
690 into the free troposphere during fire events observed with polarization lidar at Limassol,
691 Cyprus, *Atmos. Chem. Phys.*, 14(22), 12155–12165, doi:10.5194/acp-14-12155-2014, 2014.

692 Papayannis, A., Amiridis, V., Mona, L., Tsaknakis, G., Balis, D., Bösenberg, J., Chaikovski,
693 A., De Tomasi, F., Grigorov, I., Mattis, I., Mitev, V., Müller, D., Nickovic, S., Pérez, C.,
694 Pietruczuk, A., Pisani, G., Ravetta, F., Rizi, V., Sicard, M., Trickl, T., Wiegner, M., Gerding,
695 M., Mamouri, R. E., D’Amico, G. and Pappalardo, G.: Systematic lidar observations of
696 Saharan dust over Europe in the frame of EARLINET (2000–2002), *J. Geophys. Res.*,
697 113(D10), D10204, doi:10.1029/2007JD009028, 2008.

698 Paronis, D., Dulac, F., Chazette, P., Hamonou, E., and Liberti, G. L.: Aerosol optical
699 thickness monitoring in the Mediterranean, *J. Aerosol Sci.*, 29, S671–S672, 1998.

700 Randriamiarisoa, H., Chazette, P., and Megie, G.: Retrieving the aerosol single-scattering
701 albedo from the NO₂ photolysis rate coefficient, *Tellus B*, 56(2), 118–127,
702 doi:10.3402/tellusb.v56i2.16408, 2004.

703 Raut, J.-C., and Chazette, P.: Radiative budget in the presence of multi-layered aerosol
704 structures in the framework of AMMA SOP-0, *Atmos. Chem. Phys.*, 8(4), 12461–12528,
705 doi:10.5194/acpd-8-12461-2008, 2008.

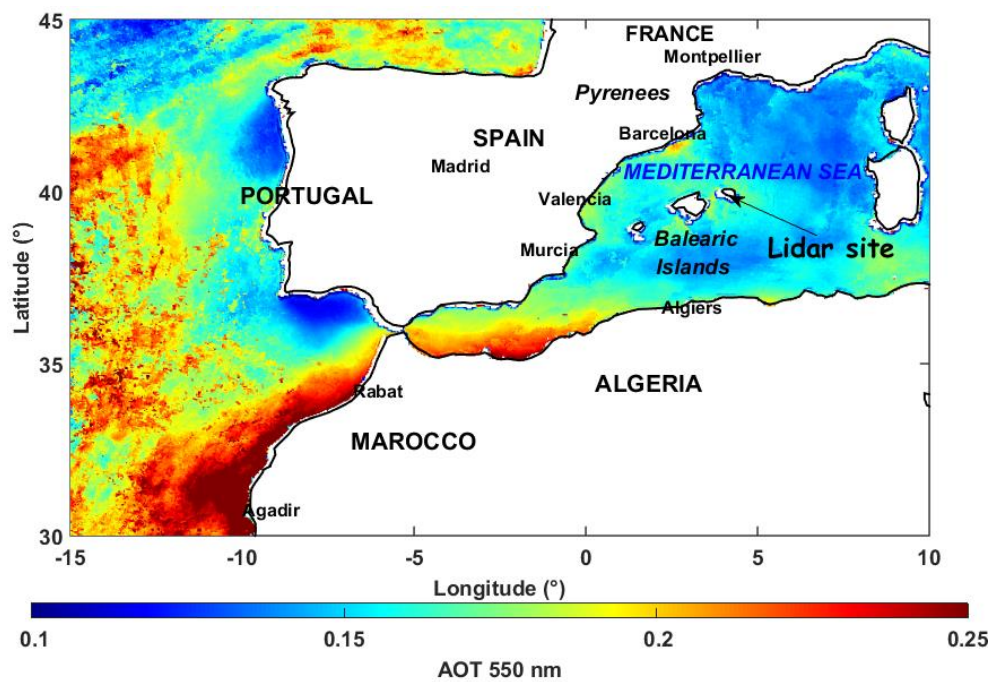
706 Royer, P., Chazette, P., Lardier, M., and Sauvage, L.: Aerosol content survey by mini N2-
707 Raman lidar: Application to local and long-range transport aerosols, *Atmos. Environ.*, 45(39),
708 7487–7495, 2011.

709 Tesche, M., Gross, S., Ansmann, A., Müller, D., Althausen, D. and Freudenthaler, V., and
710 Esselborn, M.: Profiling of Saharan dust and biomass-burning smoke with multiwavelength
711 polarization Raman lidar at Cape Verde, *Tellus B*, 63, 649–676,
712 doi:10.1111/j.16000889.2011.00548.x, 2011.

713 Thieuleux, F., Moulin, C., Bréon, F. M., Maignan, F., Poitou, J. and Tanné, D.: *Annales*
714 *Geophysicae* Remote sensing of aerosols over the oceans using MSG / SEVIRI imagery, ,
715 23(12), 1–8, 2005.

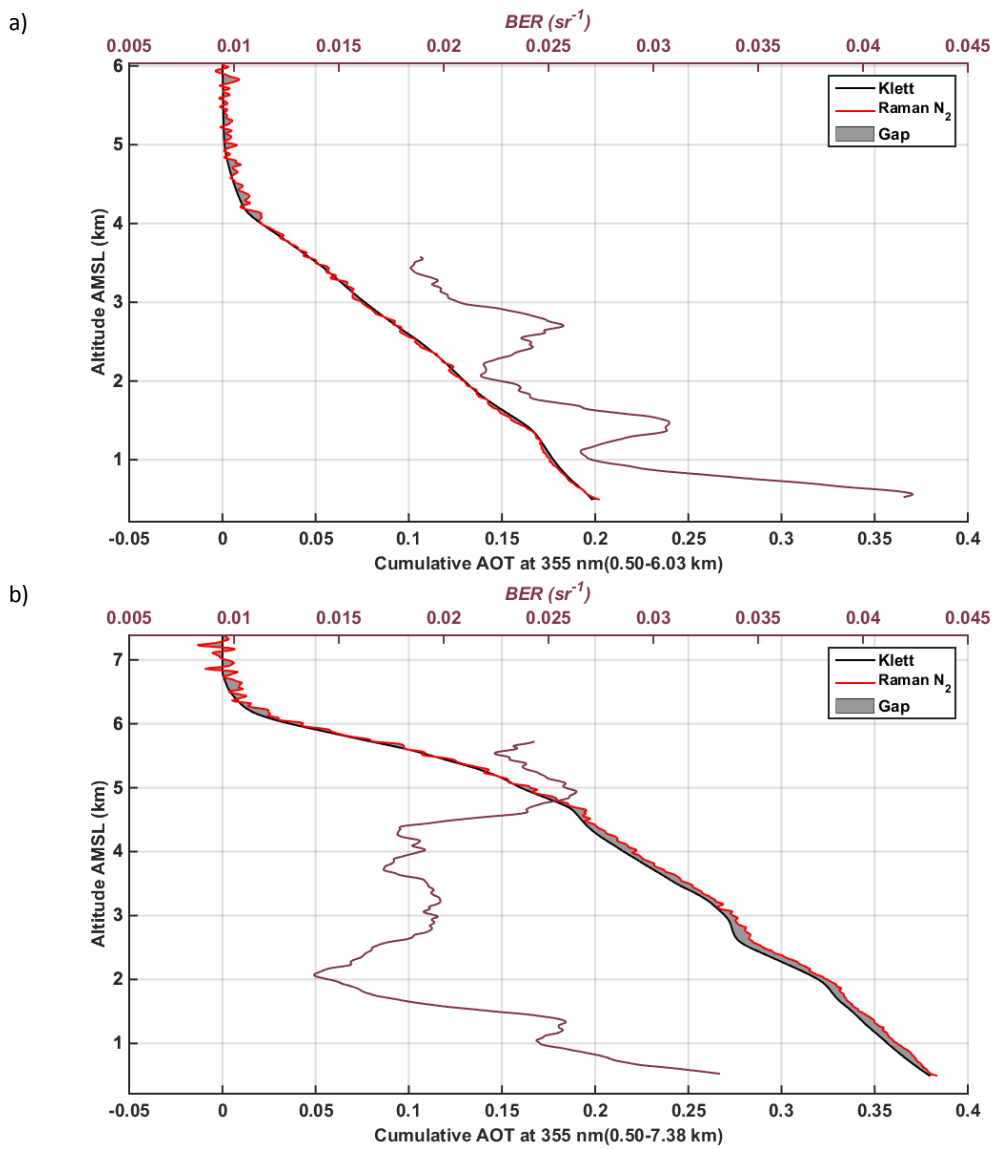
716 Thomason, L. W., Pitts, M. C., and Winker, D. M.: CALIPSO observations of stratospheric
717 aerosols: a preliminary assessment, *Atmos. Chem. Phys.*, 7, 5283-5290, 2007.

718 Vaughan, M. A., Young, S. A., Winker, D. M., Powell, K. A., Omar, A. H., Liu, Z., Hu, Y.,
719 and Hostetler, C. A.: Fully automated analysis of space-based lidar data: An overview of the
720 CALIPSO retrieval algorithms and data products, *Proc. SPIE Int. Soc. Opt. Eng.*, 5575, 16–
721 30, doi:10.1117/12.572024, 2004.

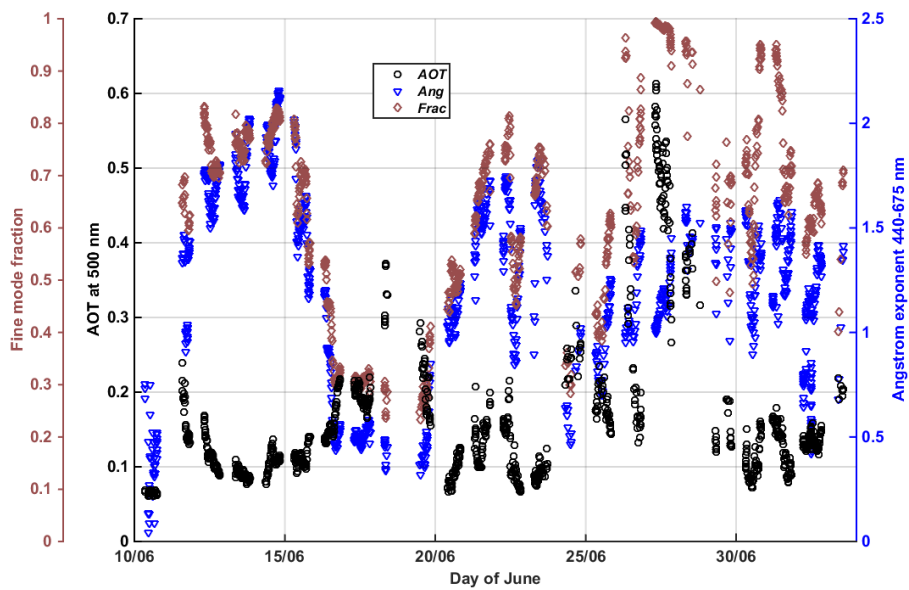


722

723 Figure 1: Location of the Cap d'en Font surface station on Menorca Island, on a map of the
 724 MSG/SEVIRI-derived aerosol optical thickness at 550 nm over ocean, averaged over the
 725 campaign period (10 June-3 July 2013, daytime).

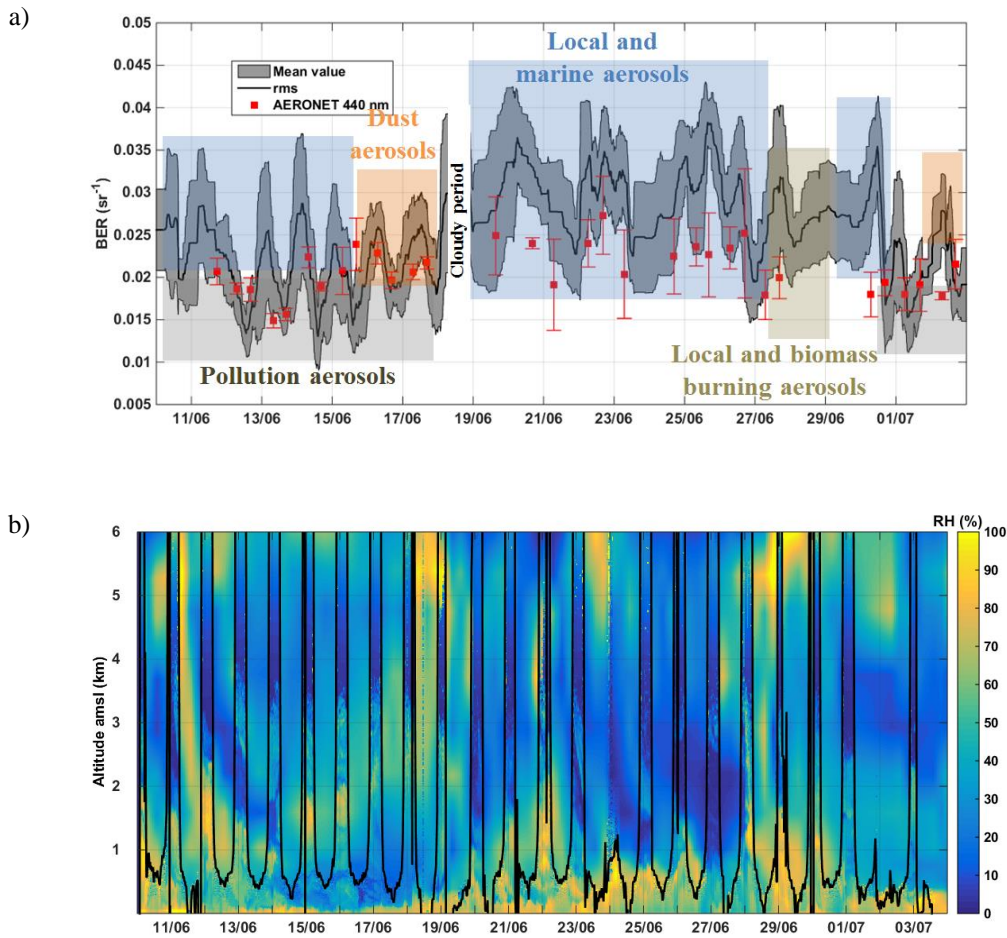


726 Figure 2: Result of the lidar inversion on the both the integrated AOT and the BER for the
 727 elastic (Klett (1985) algorithm) and N₂-Raman channels: a) the nights of 16-17 June, and b)
 728 the nights of 27-28 June. The grey area highlights the gap between the two approaches.



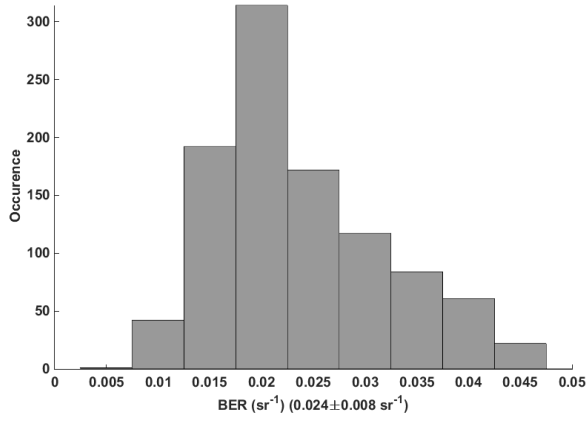
729

730 Figure 3: Temporal evolution between 10 June and 3 July 2013, local time, of the aerosol
 731 optical thickness at 500 nm (*AOT*), the Ångström exponent between 440 and 675 nm (*Ang*)
 732 and the fine mode fraction (*Frac*) as derived from the sunphotometer measurements at Cap
 733 d'en Font. The AERONET products are completed by the Microtops II manual sunphotometer
 734 measurements on 10 June.

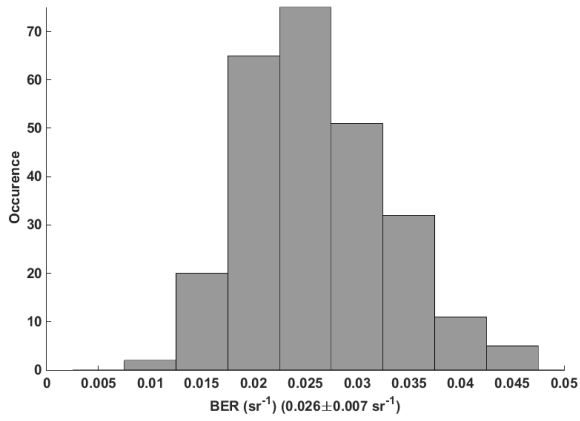


735 Figure 4: Temporal evolution of (a) the backscatter-to-extinction ratio (*BER*) and (b) the
 736 relative humidity (*RH*) between 10 and 29 June 2013. In (a) the root mean square error (*rmse*)
 737 is given by the grey area. The main aerosol categories have been identified in the figure as
 738 pollution, dust, local, marine and biomass burning aerosols using *BER* and *PDR* values (see
 739 text). The sunphotometer-derived *BER* is superimposed in red with its standard deviation
 740 (variability over half a day). In (b) the *RH* is calculated from lidar measurements using the
 741 thermodynamic temperature given by ECMWF analyses. During daytime the *RH* in the free
 742 troposphere is that of ECMWF; the boundary between the two *RH* determinations is
 743 highlighted by the continuous black line.

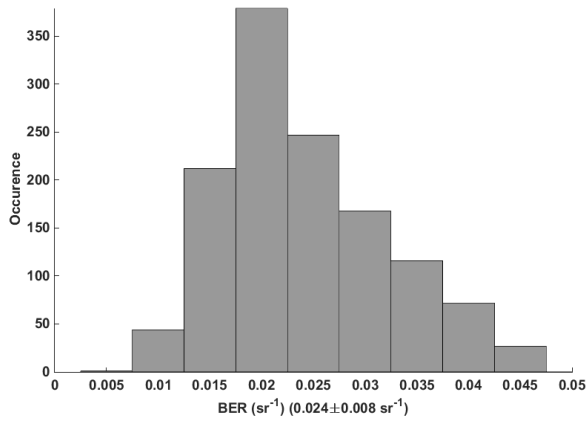
a)



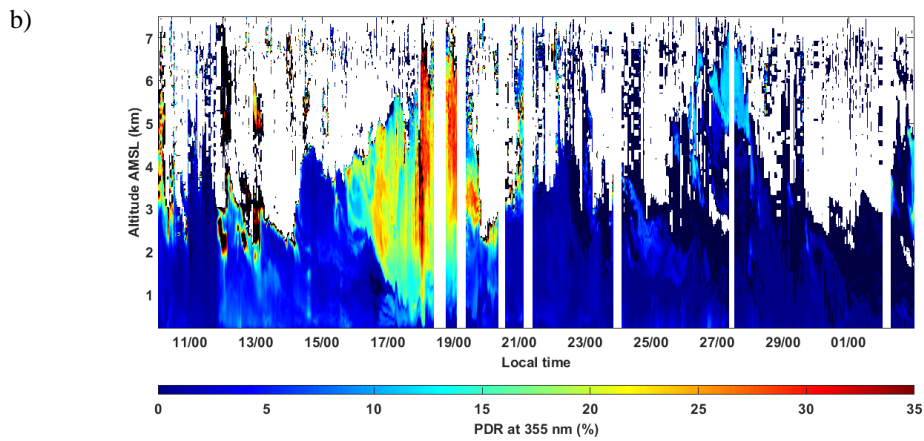
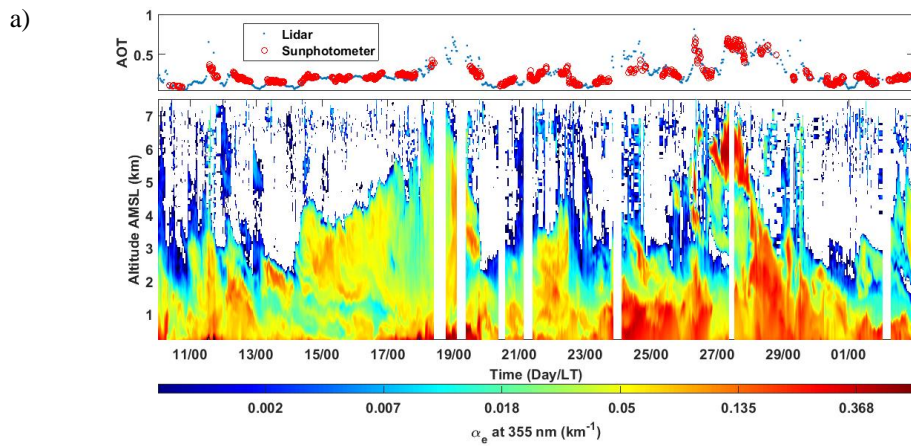
b)



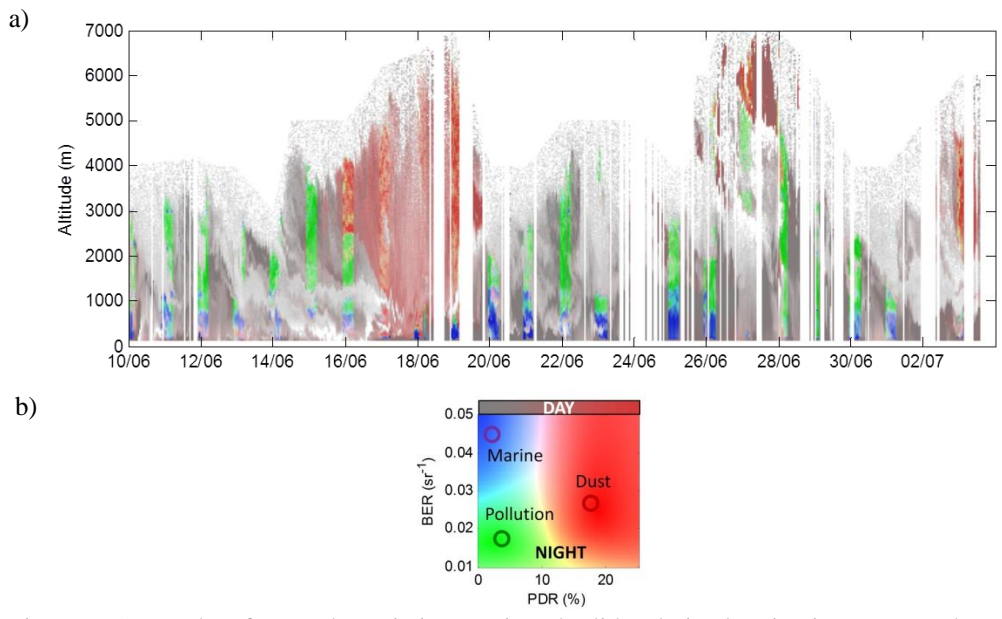
c)



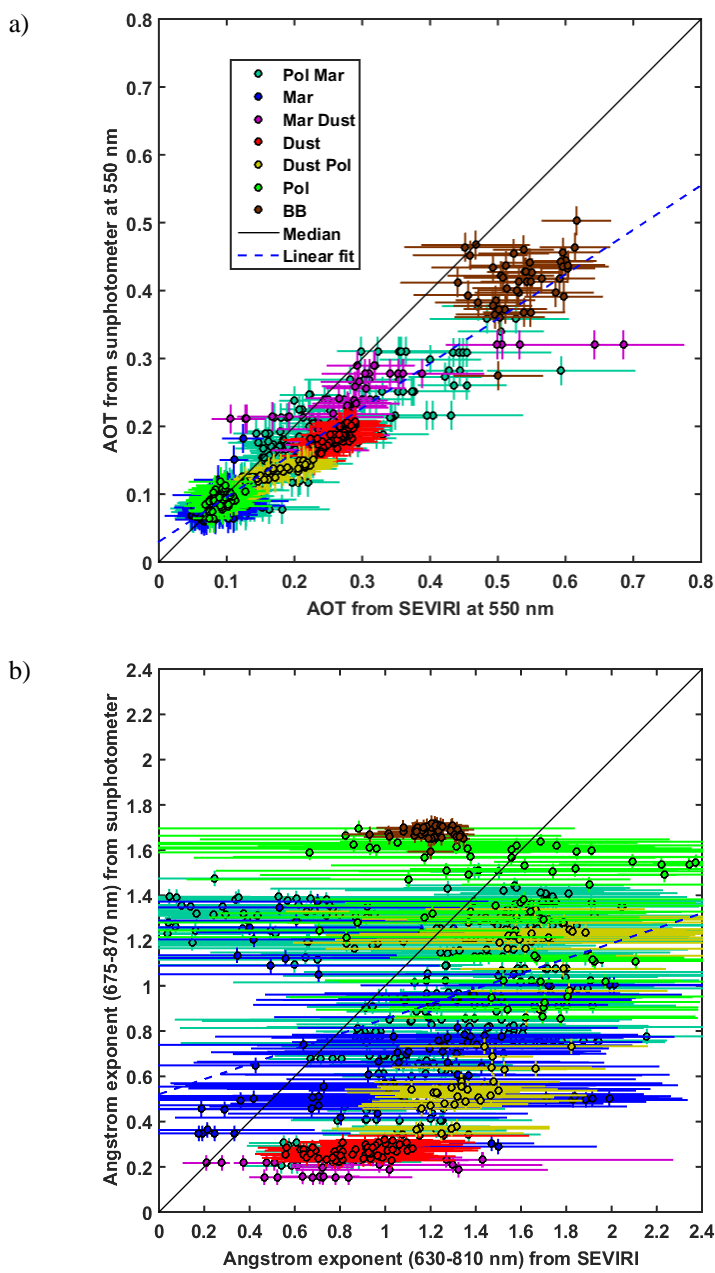
744 Figure 5: Backscatter-to-extinction ratio (*BER*) retrieved from a) the synergy of the WALI
745 lidar and the sunphotometer during daytime, b) the coupling between the elastic and N₂-
746 Raman channels during nighttime, and c) the synthesis of daytime and nighttime results.



747 Figure 6: a) The temporal evolution of the vertical profile of the aerosol extinction coefficient
 748 at 355 nm (α_e). The top panel shows AOT at 355 nm derived from the sunphotometer (red
 749 circles) and lidar measurements (blue points). b) The temporal evolution of the particulate
 750 depolarization ratio vertical profile at 355 nm (PDR). Time white stripes correspond to
 751 periods filtered out by visual examination of the lidar signal to identify the occurrence of
 752 clouds.

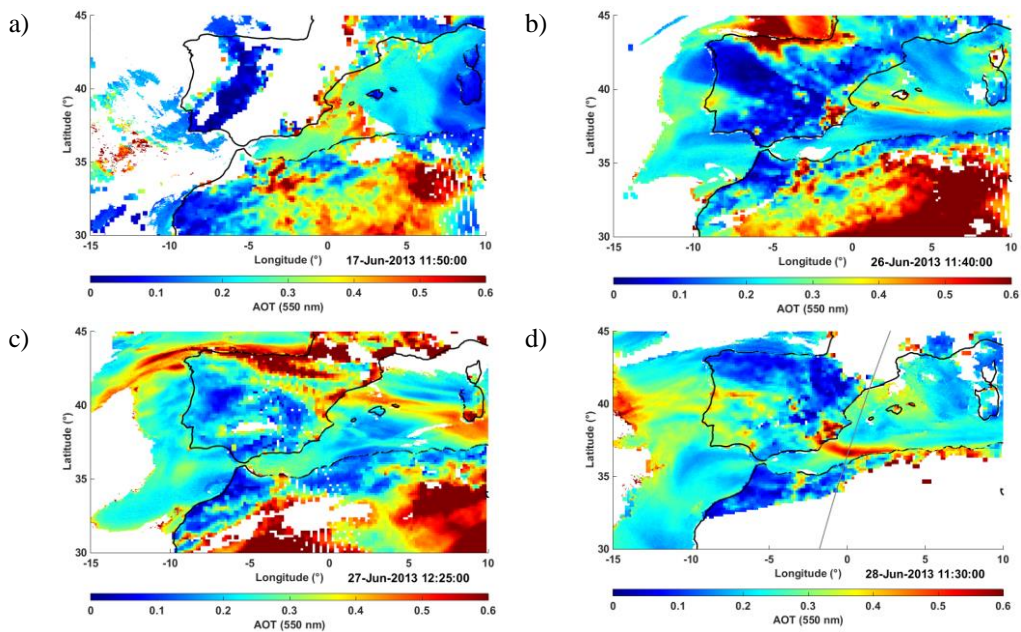


753 Figure 7: a) Results of aerosol speciation as given by lidar-derived extinction, PDR and BER,
 754 with backscatter coefficient coded as saturation (no saturation, white = 0, full saturation = 5
 755 | $10^{-6} \text{ m}^{-1} \cdot \text{sr}^{-1}$); b) Key for the colours of the above. Nighttime: dust-, pollution- and marine-like
 756 aerosols coded as red, green and blue respectively. Daytime: PDR coded as the saturation of
 757 red (top of the colour key). Intermediate colours and grey thus designate undetermined layers
 758 where aerosol mixing may occur.

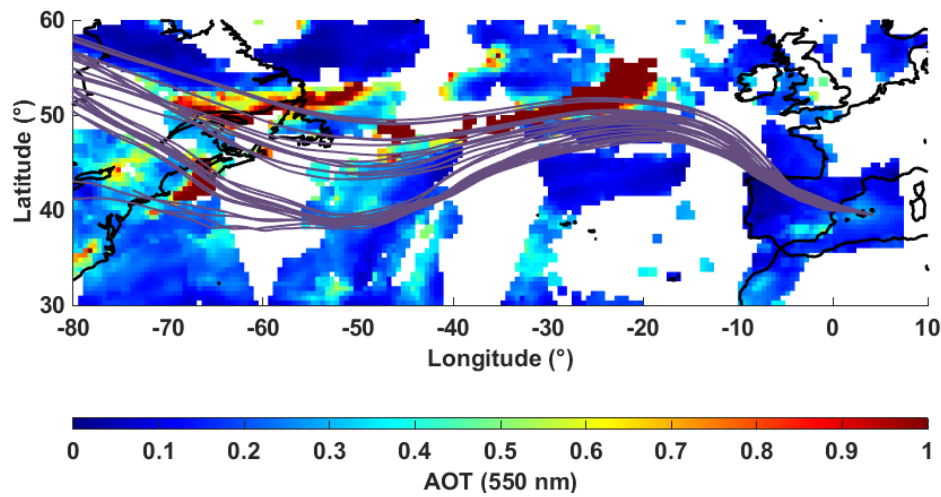


759 Figure 8: a) Scatter plots between SEVIRI and the ground-based sunphotometer of Menorca
 760 for the aerosol optical thickness AOT at 550 nm. The dotted line corresponds to the best fit
 761 against both retrievals. b) The Ångström exponent for similar spectral ranges. A total of 846
 762 coincident data pairs between 10 and 30 June are available for comparison. To the four

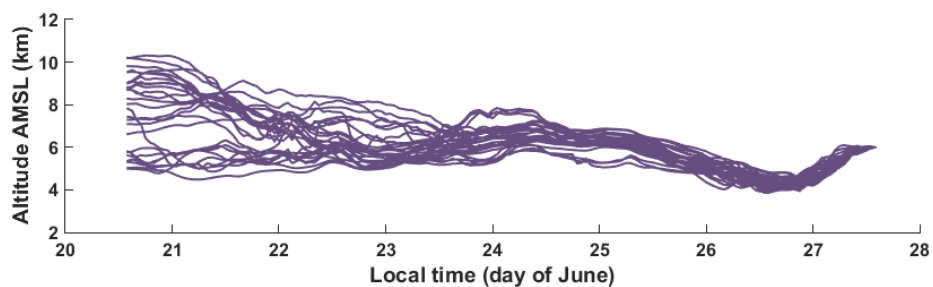
763 | aerosol types identified in **Figure 7** are added 3 mixed types which are all distinguished by
764 | their colour: pollution (Pol), dust (Dust), marine (Mar) and biomass burning (BB), mixing of
765 | pollution and marine (Pol Mar), Marine and dust (Mar Dust), dust and pollution (Dust Pol).
766 | The solid curve represents the centroid of the distribution.



767 Figure 9: AOT composition between the MODIS observations over land and SEVIRI over
 768 sea. The SEVIRI AOT was corrected by a factor 0.65 as identified from comparisons with the
 769 sunphotometer reported in Figure 8. Top-left panel (a) is for 17 June, top-right (b) for 26 June,
 770 bottom-left (c) for 27 June, and bottom-right (d) for 28 June. For 28 June the nighttime
 771 CALIOP ground track (at about 2 UTC) is marked by a continuous grey line.



772



773

774 Figure 10: 27 back trajectories from Menorca (39°51'44"N, 4°15'30"E). The back trajectories
 775 have been computed using the ensemble mode of the HYSPLIT model (courtesy of NOAA
 776 Air Resources Laboratory; <http://www.arl.noaa.gov>). The end location of the air mass
 777 trajectories is at 6 km amsl in the plume detected by the WALI lidar on 27 June, 2013 over
 778 Menorca (see Figure 6a). The top panel presents the location of each back trajectory
 779 superimposed over the MODIS-derived AOT at 550 nm of 24 June, 2013, for several orbits.
 780 The bottom panel shows the altitude of the back trajectories against time.